nature sustainability

Article

https://doi.org/10.1038/s41893-022-01028-x

All-temperature zinc batteries with high-entropy aqueous electrolyte

Received: 10 December 2021

Accepted: 23 November 2022

Published online: 09 January 2023

Check for updates

Chongyin Yang[1,2,11], Jiale Xia[1,11], Chunyu Cui[1,11], Travis P. Pollard[3], Jenel Vatamanu[3], Antonio Faraone[4], Joseph A. Dura[4], Madhusudan Tyagi[4,5], Alex Kattan[6], Elijah Thimsen[6], Jijian Xu[1], Wentao Song[2], Enyuan Hu[7], Xiao Ji[1], Singyuk Hou[1], Xiyue Zhang[1], Michael S. Ding[3], Sooyeon Hwang[8], Dong Su[8], Yang Ren[9,10], Xiao-Qing Yang[7], Howard Wang[5], Oleg Borodin[3] ✉ & Chunsheng Wang[1] ✉

Electrification of transportation and rising demand for grid energy storage continue to build momentum around batteries across the globe. However, the supply chain of Li-ion batteries is exposed to the increasing challenges of resourcing essential and scarce materials. Therefore, incentives to develop more sustainable battery chemistries are growing. Here we show an aqueous $ZnCl_2$ electrolyte with introduced LiCl as supporting salt. Once the electrolyte is optimized to $Li_2ZnCl_4{\cdot}9H_2O$, the assembled Zn–air battery can sustain stable cycling over the course of 800 hours at a current density of 0.4 mA cm^{-2} between −60 °C and +80 °C, with 100% Coulombic efficiency for Zn stripping/plating. Even at −60 °C, >80% of room-temperature power density can be retained. Advanced characterization and theoretical calculations reveal a high-entropy solvation structure that is responsible for the excellent performance. The strong acidity allows $ZnCl_2$ to accept donated Cl^- ions to form $ZnCl_4^{2-}$ anions, while water molecules remain within the free solvent network at low salt concentration or coordinate with Li ions. Our work suggests an effective strategy for the rational design of electrolytes that could enable next-generation Zn batteries.

Environmental and resource sustainability have become increasingly important for the development of next-generation battery technologies needed to meet the ever-expanding market for renewable energy storage in smart grids and electrification of vehicles[1,2]. Li-ion battery (LIB) technologies dominate in this space currently due to their high energy density and long cycle life. However, as demand for energy storage capacity continues to accelerate, price and resource volatility due to limitations in the supply of lithium and transition metals are garnering more attention. In addition, LIBs require an energy-intensive manufacturing process, often utilizing toxic and environmentally unfriendly chemicals. The potential safety issues during LIB operation and their tolerance to mechanical abuse are also not completely resolved.

Aqueous zinc batteries have emerged as one of the promising complementary chemistries because of the potential for zinc (Zn)

[1]Department of Chemical and Biomolecular Engineering, University of Maryland, College Park, MD, USA. [2]Department of Physics and Atmospheric Science, Dalhousie University, Halifax, NS, Canada. [3]Battery Science Branch, DEVCOM Army Research Laboratory, Adelphi, MD, USA. [4]NIST Center for Neutron Research, National Institute of Standards and Technology, Gaithersburg, MD, USA. [5]Department of Materials Science and Engineering, University of Maryland, College Park, MD, USA. [6]Department of Energy, Environmental and Chemical Engineering, Washington University, St Louis, MO, USA. [7]Chemistry Division, Brookhaven National Laboratory, Upton, NY, USA. [8]Center for Functional Nanomaterials, Brookhaven National Laboratory, Upton, NY, USA. [9]X-ray Science Division, Advanced Photon Source, Argonne National Laboratory, Argonne, IL, USA. [10]Department of Physics, City University of Hong Kong, Kowloon, Hong Kong, China. [11]These authors contributed equally: Chongyin Yang, Jiale Xia, Chunyu Cui. ✉e-mail: oleg.a.borodin.civ@army.mil; cswang@umd.edu

anode to be made compatible with aqueous electrolytes. Zn is relatively abundant and has a mature recycling infrastructure. Recent application of 'water-in-salt' electrolytes has extended the electrochemical stability window of aqueous electrolytes[3,4] and enabled new battery chemistries[5,6], including zinc batteries that are presently limited to primary use[7,8]. However, the benefits of water-in-salt electrolytes for use in aqueous zinc batteries are not enough to overcome barriers to commercialization due to underwhelming reversibility of Zn plating/stripping, insufficient energy efficiency and poor transport at low temperatures.

Different from simply increasing salt concentration in a single-salt electrolyte, the addition of concentrated supporting salts has proved to be another promising strategy to largely exclude water from solvating Zn^{2+} in aqueous electrolytes[9–11]. As a result, such electrolytes exhibit a substantial decrease in hydrolysis and a corresponding increase in the reversibility of Zn plating/stripping. However, its potential of improving low-temperature ionic transport has not been systematically explored as any remaining 'free water' in electrolyte might freeze at low temperature.

In this work, we report on the addition of lithium chloride (LiCl) as a supporting salt into a zinc chloride ($ZnCl_2$) aqueous electrolyte to form $Li_2ZnCl_4{\cdot}RH_2O$ with varying R. Waters either remain as part of the free solvent network at low salt concentration or are preferentially coordinated by Li^+ ions, eliminating free water as salt concentration increases, while Cl^- ions preferentially form $ZnCl_4^{2-}$ anions or small $[ZnCl_{4-m}^{2-m}]_n$ anion clusters (m = 0, 1 or 2, i.e. the neighboring Zn cations are sharing by 1 Cl or 2 Cl; $n \leq 3$). The length of these anionic clusters is limited by an increase in Li–Cl contacts appearing as R decreases, which preserves a high ionic conductivity[12]. Optimizing R, the $Li_2ZnCl_4{\cdot}9H_2O$ electrolyte maximizes the degree of frustration to deliver a high-entropy electrolyte (HEE), simultaneously suppressing hydrolysis and crystallization at low temperature. This HEE enables a zinc–air battery to achieve an unprecedented cycling stability at operating temperatures between −60 and +80 °C, providing ~100% Coulombic efficiency for Zn stripping/platting and >80% of the room-temperature power density at −60°C with excellent cycling stability.

Results

All-temperature transport properties of HEE

In dilute salt-in-solvent electrolytes, all ions tend to be solvated by highly polar solvents (bottom left of Fig. 1a). The strong dipolar interactions between solvent molecules promote structural ordering, resulting in a high glass transition temperature (T_g)[13] or freezing point[14]. As an example, electrolyte viscosity (η) of 2 mol kg^{-1} LiCl or 2 mol kg^{-1} $ZnCl_2$ aqueous single-salt electrolytes increases rapidly as temperature decreases, as shown by the early rollover of ionic conductivities at >−20 °C (Fig. 1b). Their deviation from the Vogel–Tammann–Fulcher (VTF) equation[15] (corresponding dash lines) is due to the spontaneous increase of salt concentration caused by water crystallizing into ice. Adding non-polar or low-polarity solvents with low melting points into salt-in-solvent electrolytes can reduce their viscosity even at a low temperature. However, it also reduces the overall dielectric constant and the concentration of charge carriers[16,17], thereby decreasing ionic conductivity. Alternatively, it is well known that switching to the super-concentrated or 'solvent-in-salt' regime disrupts the intermolecular network in free solvent clusters (bottom right of Fig. 1a)[12]. As a result, the substantially reduced solvent activity suppresses the contraction and crystallization of solvent clusters at a low temperature. However, its high cation/solvent ratio also introduces contact ion pairs and salt aggregates[18], as evidenced by the sudden drop of ionic conductivities for aqueous $LiCl{\cdot}3H_2O$ and $ZnCl_2{\cdot}3H_2O$ at −20 °C (Fig. 1b), resulting in salt/solvate precipitation and destabilization of the global structure at a low temperature. Both conventional solvent-in-salt and salt-in-solvent electrolytes contain local cluster structures with high structural ordering, limiting the ionic conductivity at a low temperature.

In the $Li_2ZnCl_4{\cdot}RH_2O$ electrolyte proposed as a HEE here, the hydrated Li^+ cation–$ZnCl_4^{2-}$ anion pair size[19] is larger than Bjerrum critical radius in aqueous solution[20], indicating dissociation of Li^+ from the $ZnCl_4^{2-}$ complex (middle of Fig. 1a). Meanwhile, the suppressed ion pairing means that Li^+ remains largely hydrated even in the highly concentrated regime, serving as a water sponge to break down the hydrogen-bond network of water[21]. Figure 1b shows the extraordinary conductivity retention of $Li_2ZnCl_4{\cdot}9H_2O$ electrolyte in a temperature range from +80 to −80 °C, compared with single-salt aqueous electrolytes of $LiCl{\cdot}3H_2O$ or $ZnCl_2{\cdot}3H_2O$ with the same salt/water ratio = 1/3 and their diluted versions with molar concentrations of 2 mol kg^{-1}. The ionic conductivity of $Li_2ZnCl_4{\cdot}9H_2O$ exactly follows the VTF equation across the whole temperature range, dropping from 200 mS cm^{-1} at +80 °C to 1.36 and 0.66 mS cm^{-1} at the low temperatures of −70 and −80 °C, respectively, which is superior to competing electrolytes developed for low-temperature operations[16,17]. Supplementary Fig. 1 highlights the liquid state of $Li_2ZnCl_4{\cdot}6H_2O$ and $Li_2ZnCl_4{\cdot}9H_2O$ at −70 °C. Its Vogel temperature, T_0, equal to the glass transition in ideal glasses[22], is 12 °C lower than the measured T_g (−109 °C; Supplementary Table 1). This suggests that $Li_2ZnCl_4{\cdot}9H_2O$ is a fragile glass former without any crystalline phase transition of water or salt in this temperature range, which is rare in aqueous systems[23]. As a result, $Li_2ZnCl_4{\cdot}9H_2O$ is the only electrolyte without any thermal hysteresis in the cooling–heating cycle between +80 and −80 °C (red line in insert of Fig. 1b), which is critical for battery performance in harsh environments. Further studies of various concentrated $Li_2ZnCl_4{\cdot}RH_2O$ electrolyte systems showed similar ionic conductivity with R from 6 to 18 (Supplementary Fig. 2a). The Zn-ion transference number t_{Zn} at room temperature was found to range from 0.41 to 0.25 for R = 9 and R = 6 in $Li_2ZnCl_4{\cdot}RH_2O$ at 20 °C (Supplementary Fig. 2b,c). Interestingly, t_{Zn} decreases slowly with temperature for all concentrations, while the Li-ion transference number t_{Li} for R = 9 is relatively stable at ~0.3 over the whole temperature range.

$Li_2ZnCl_4{\cdot}RH_2O$ electrolytes show unexpected properties due to their unique solvation structure. We evaluated the overall ionic conductivities of $Li_xZn_{3-x}Cl_{6-x}{\cdot}9H_2O$ with different molar ratios of LiCl/$ZnCl_2$ and at different temperatures (Fig. 1c). $Li_2ZnCl_4{\cdot}9H_2O$ ($n_{LiCl}/n_{ZnCl_2} = 2$) showed the highest ionic conductivity in the temperature range from +20 °C to −70 °C (Fig. 1c), which also agreed with the T_g (red dashed line in Fig. 1c) measured using differential scanning calorimetry (DSC; Supplementary Table 1). The extra Cl^- donated from the LiCl supporting salt to $ZnCl_2$ satisfies the preferred tetrahedral coordination structure of $ZnCl_4^{2-}$ anions, reducing the prevalence of edge-shared Cl^- between Zn^{2+}. This, in combination with disruption by partially hydrated Li–Cl contacts discussed later, limits the formation of contiguous $[ZnCl_{4-m}^{2-m}]_n$ ($n > 3$) extended networks, resulting in a high degree (~0.5) of ion uncorrelated motion (ionicity) at room temperature (Supplementary Fig. 2d). The formation of these extended networks is a noted issue in concentrated single-salt $ZnCl_2{\cdot}RH_2O$ that limits conductivity[24]. Changes to the solvation structure in the $Li_2ZnCl_4{\cdot}RH_2O$ electrolytes appear to maximize for the LiCl/$ZnCl_2$ molar ratio of 2/1, leading to the formation of what we term high-entropy electrolyte, characterized by a maximum in the competition between the dissociation of LiCl salts, breaking up extended $[ZnCl_{4-m}^{2-m}]_n$ ($n > 3$) aggregates into wide distribution of shorter aggregates ($n \leq 3$), disruption of the free solvent hydrogen-bond network and exclusion of water from Zn^{2+} solvation[25,26].

Interestingly, due to the mechanism of frustration discussed in the preceding, the Walden plot for $Li_2ZnCl_4{\cdot}RH_2O$ electrolytes shows some deviation from the Walden rule (Supplementary Information)[27]. Near room temperature in Fig. 1d, $Li_2ZnCl_4{\cdot}9H_2O$ shows sub-ionic behaviour in accordance with highly concentrated aqueous systems due to ion pairing[28]. However, the plot of $Li_2ZnCl_4{\cdot}9H_2O$ approaches the ideal 'KCl line' as temperature (or η^{-1}) decreases. This indicates that after eliminating ice nucleation and salt recrystallization, charge motion

https://doi.org/10.1038/s41893-022-01028-x

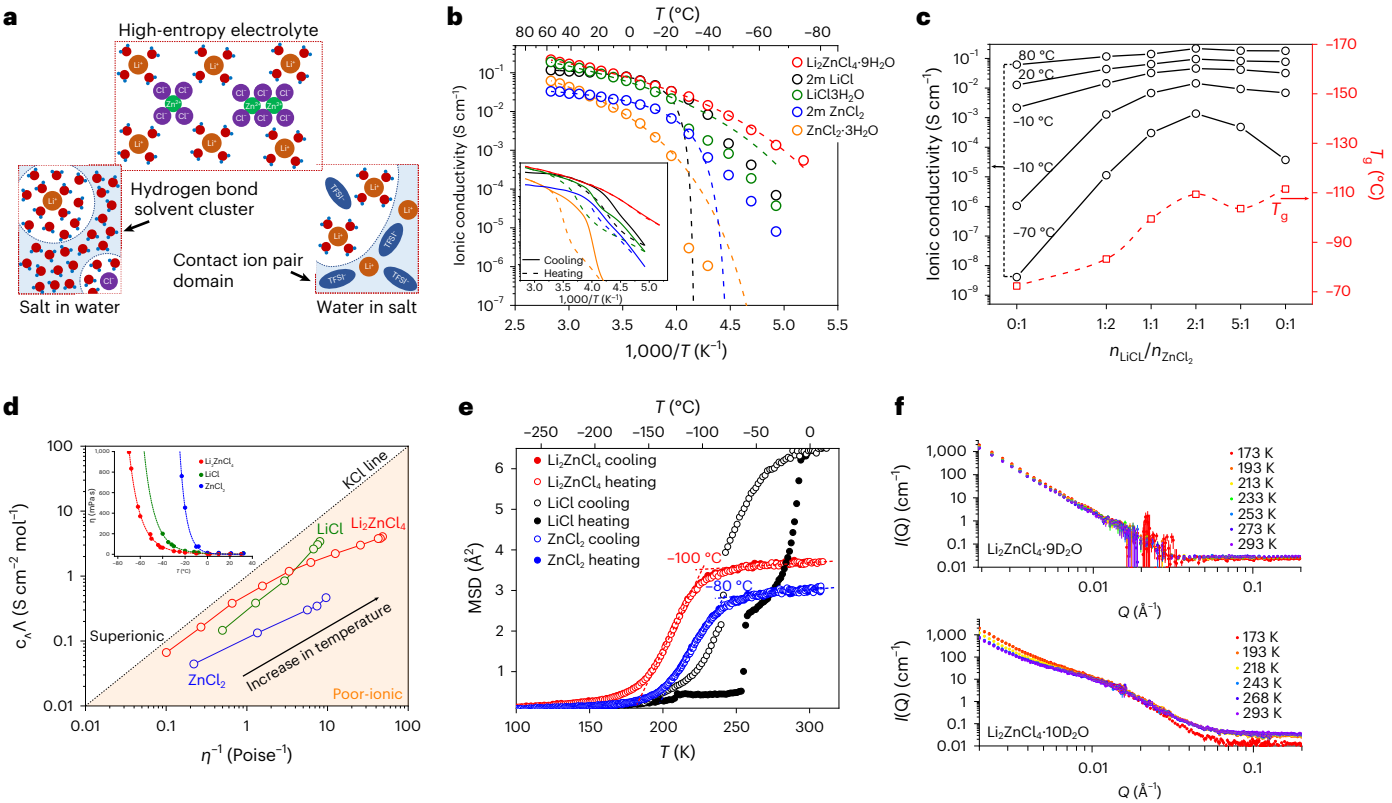

Fig. 1 | Transport properties over wide temperature window. a, Illustration of solution structure in different electrolytes. **b**, Arrhenius plots of the overall ionic conductivities of $Li_2ZnCl_4·9H_2O$ electrolyte compared with concentrated $LiCl·3H_2O$, $ZnCl_2·3H_2O$ solutions and dilute (2 mol kg^{-1}) LiCl and $ZnCl_2$ aqueous solutions. Circles, experimental data; dashed lines, the fitting curves of VTF equation. Insert shows the hysteresis loops (same colours as in the main figure) for each electrolyte during the measurement cycle with a cooling course (solid lines, 80 °C → −70 °C), then a heating course (dashed lines, −70 °C → 80 °C), with an equilibrium time of 5 h for each temperature. **c**, The overall ionic conductivities (solid lines) of $LiCl–ZnCl_2–9H_2O$ solutions with different $LiCl/ZnCl_2$ ratios from 0/1 to 1/0 at different temperatures. The glass transition temperatures (T_g) measured by DSC are shown as dashed line. **d**, Walden plot for the $Li_2ZnCl_4·9H_2O$, $LiCl·3H_2O$ and $ZnCl_2·3H_2O$ electrolytes at the temperature range from +80 to −70 °C. The prefactor C_Λ is 5/3 for $Li_2ZnCl_4·9H_2O$, 1 for $LiCl·3H_2O$ and 3 for $ZnCl_2·3H_2O$ (see detail calculation in Supplementary Information). In a Walden plot, electrolyte solutions can be classified in terms of their performance as ionic conductors: superionic (upper-left region above the ideal KCl line), good-ionic (on the ideal line), sub-ionic (bottom right region under the ideal line) or non-ionic (far below the ideal line) liquids and solutions. Insert shows viscosity of these electrolytes as functions of the temperatures. **e**, Temperature dependence of MSD of $Li_2ZnCl_4·9H_2O$, $LiCl·3H_2O$ and $ZnCl_2·3H_2O$ solutions measured by fixed window scan with HFBS. **f**, SANS intensity profile for $Li_2ZnCl_4·9D_2O$ and $Li_2ZnCl_4·10D_2O$ at different temperatures (173 K–293 K). Data are presented as mean values ± standard error of the mean. Error bars represent standard error propagation from the counting statics of the measurements (square root of the number of neutrons scattered at that Q).

in the $Li_2ZnCl_4·9H_2O$ electrolyte becomes less correlated, translating to superior transport properties at low temperatures.

The dynamics of water at low temperatures in $Li_2ZnCl_4·9H_2O$, $LiCl·3H_2O$ and $ZnCl_2·3H_2O$ electrolytes on timescales of ~100 ps^{-2} ns was probed using high-flux neutron backscattering spectrometry (HFBS). As shown in Fig. 1e, the mean square displacement (MSD) of water in $Li_2ZnCl_4·9H_2O$ is nearly constant down to −60 °C. The MSD falls off rapidly at −100 °C, which is close to T_g (−110 °C; Fig. 1c). By contrast, the MSDs of $LiCl·3H_2O$ and $ZnCl_2·3H_2O$ started to drop at −25 °C, which correlates with their deviations from VTF behaviour (Fig. 1b). The MSD for $LiCl·3H_2O$ showed hysteresis due to water crystallization observed at −30 °C in cooling and melting at −10 °C in heating in accordance with the hysteresis observed in conductivity (Fig. 1b insert), while both $Li_2ZnCl_4·9H_2O$ and $ZnCl_2·3H_2O$ showed no hysteresis during the cooling and heating cycle. This observation indicates that the hysteresis in ionic conductivity observed for $ZnCl_2·3H_2O$ (insert in Fig.1b) is due to changes of the $[ZnCl_{4-m}^{2-m}]_n$ aggregates and is not correlated with water MSD.

The subtle microscopic structure changes of water at low temperature were also evaluated using small-angle neutron scattering (SANS), using D_2O to enhance sensitivity. Figure 1f demonstrated that $Li_2ZnCl_4·9D_2O$ and $Li_2ZnCl_4·10D_2O$ electrolytes show a typical power-law behaviour at low Q (wave vector transfer of neutron), indicative of a homogeneous fractal structure at length scales >100 nm. The linear (in log–log scale) scattering profiles for the $Li_2ZnCl_4·9D_2O$ electrolyte showed no temperature dependence during cooling from 293 K to 173 K, indicating that a homogeneous liquid phase remained and no ice nucleation occurred across the investigated temperature range[29]. As a reference, sudden changes happened below 213 K for $LiCl·3D_2O$ and $ZnCl_2·3D_2O$ (Supplementary Fig. 3), which correlated with the observed changes in ionic conductivity (Fig. 1b) and dynamic measurements (Fig. 1e).

Characterization of high-entropy solvation structure

Density functional theory- (DFT-) based Born–Oppenheimer molecular dynamics (BOMD) simulations and polarizable force-field-based molecular dynamics (FF-MD) simulations provided further insight into the structure and transport for single-salt and bi-salt electrolytes (Fig. 2). The structures of $Li_2ZnCl_4·9H_2O$, $Li_2ZnCl_4·6H_2O$ and $LiCl·3H_2O$ electrolytes predicted by molecular dynamics (MD) simulations were in excellent agreement with high-energy X-ray scattering measurements (Fig. 2b and Supplementary Fig. 4a–c). BOMD and FF-MD simulations of $Li_2ZnCl_4·RH_2O$ showed the Zn–Cl coordination number remained fixed ~4 independent of water concentration from $R = 15$ to $R = 6$ (green

https://doi.org/10.1038/s41893-022-01028-x

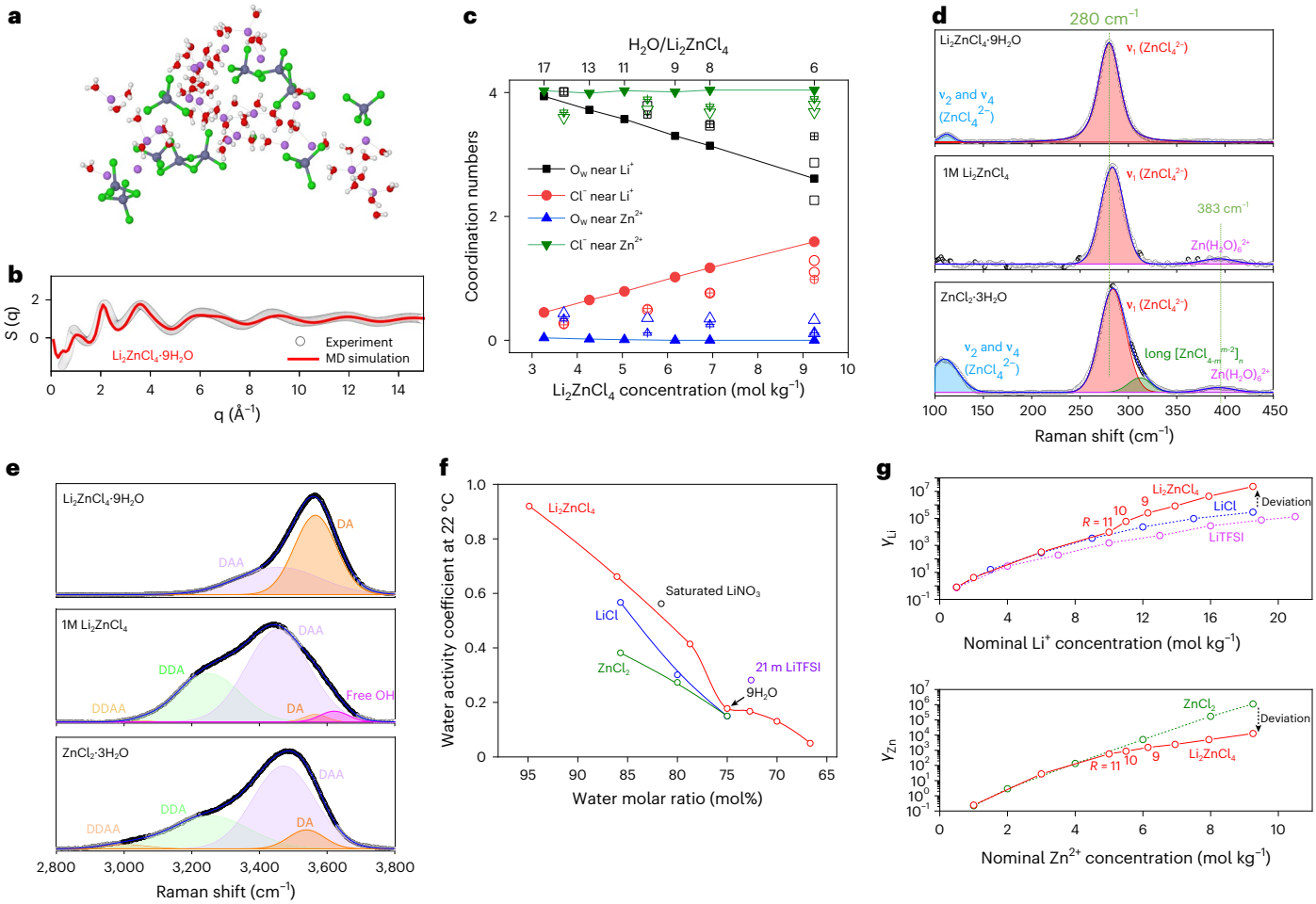

Fig. 2 | Solvation structure. a, A representative configuration of $[ZnCl_{4-m}^{2-m}]_n$ anions ($n \leq 3$, green and grey network) and water (red and white) coordinating nearby Li^+ cations (shown as purple) from MD simulations of $Li_2ZnCl_4{\cdot}9H_2O$ electrolyte; the Zn–Cl bonds and Li–O(water) dashed lines are shown when the Zn–Cl^- and Li^+–O(water) distances are less than 2.8 Å. **b**, High-energy X-ray scattering spectra of $Li_2ZnCl_4{\cdot}9H_2O$ measured by synchrotron and predicated by MD simulation. **c**, The number of water oxygen (O_w) and Cl^- within 2.8 Å of Zn^{2+} and Li^+ from MD simulations using modified atomic multipole optimized energetics for biomolecular simulation (AMOEBA) force field (filled symbols) at 25 °C for $Li_2ZnCl_4{\cdot}RH_2O$ electrolytes; the coordination numbers from the last 20 ps of BOMD simulations for replica *r*1 using PBE-D3BJ and revPBE-D3BJ functionals at 177 °C are given as open and crossed open symbols, respectively. **d**,**e**, Raman spectra of $Li_2ZnCl_4{\cdot}RH_2O$ at the Raman shift range of 100–450 cm^{-1} (**d**) and 2,800–3,800 cm^{-1} (**e**). All the Raman bands are fitted by Gaussian peaks with coefficient of determination $R^2 > 0.999$. **f**, The activity coefficient of water as a function of water molar fractions estimated by vapour-pressure measurement at 22 °C. **g**, The activity coefficients for Li^+ (upper) and Zn^{2+} (lower) as a function of their concentrations in various aqueous solutions estimated by the equilibrium potential shift of Li_xFePO_4 ($x = 0.5$) and Zn metal electrodes, respectively.

symbols in Fig. 2c), while barely any water (≤0.2) is observed in the first solvation shell of Zn (blue symbols in Fig. 2c). The $ZnCl_2{\cdot}RH_2O$ ($R = 4$–17) single-salt electrolyte also showed a preference for Cl^- approaching over water in the Zn^{2+} first solvation shell (Supplementary Fig. 4d), in good agreement with previous reports[24,30–32]. However, water is not completely excluded from the Zn^{2+} solvation shell in single-salt electrolyte with Zn^{2+} being hydrated by 0.4–1.0 waters in $ZnCl_2{\cdot}RH_2O$. The extended $[ZnCl_{4-m}^{2-m}]_n$ ionic networks ($n > 3$) in $ZnCl_2{\cdot}RH_2O$ break up into smaller anions $ZnCl_4^{2-}$ and short $[ZnCl_{4-m}^{2-m}]_n$ chains ($n \leq 3$) in $Li_2ZnCl_4{\cdot}RH_2O$ with the help of extra Cl^- donated by the added LiCl salt. They are bridged via the halogen and mobile Li^+ hydrates that act as 'water sponges' in $Li_2ZnCl_4{\cdot}RH_2O$ (Supplementary Fig. 5a). The number of coordinated Cl^- with Li^+ showed an increase with increasing salt concentration but remained below 1.3 even for the most concentrated electrolyte ($R = 6$), which reflects a maximization in the dissociation of Li^+–$ZnCl_4^{2-}$ pairs (Supplementary Figs. 5–7 and extended discussion in Supplementary Information). This level of mutual frustration between hydrogen bond network of water molecules and Li^+–$ZnCl_4^{2-}$ ion pairs guarantees a high-entropy solvation structure as expected.

The formation of $ZnCl_4^{2-}$ complex anions and hydrated Li^+ cation in $Li_2ZnCl_4{\cdot}RH_2O$ electrolytes was also confirmed by Raman spectroscopy between 100 cm^{-1} and 450 cm^{-1} (Fig. 2d). Two fitted Gaussian peaks at 110 cm^{-1} (component of ν_2 and ν_4 modes) and 280 cm^{-1} (ν_1 modes) in $Li_2ZnCl_4{\cdot}9H_2O$ were assigned to the characteristic vibrational mode of zinc tetrachloride – $ZnCl_4^{2-}$ (refs. 33,34). Crucially, the Zn–O peak attributed to $[Zn(OH_2)_6]^{2+}$ at 383 cm^{-1} is absent in $Li_2ZnCl_4{\cdot}9H_2O$. When the salt was diluted to 1 mol kg^{-1}, the $ZnCl_4^{2-}$ ν_1 modes were still dominant but shifted slightly to 283 cm^{-1}, and a small peak at 383 cm^{-1} related to the hexahydrate species appeared. Interestingly, $ZnCl_2{\cdot}3H_2O$ still showed the same $[Zn(OH_2)_6]^{2+}$ peak even though the Zn^{2+}/H_2O ratio increased to 1/3 along with an extra peak for ν_1 modes of long $[ZnCl_{4-m}^{2-m}]_n$ aggregation. The coexistence of hydrated Zn^{2+} and di-, tri- and tetrachloro complexes in the $ZnCl_2$ electrolyte confirmed the lack of sufficient Cl^- to satisfy tetrahedral $ZnCl_4^{2-}$, which drives formation of large Zn–Cl network aggregates as predicted by BOMD simulation (Supplementary Fig. 5). The Raman band between 2,800 cm^{-1} and 3,800 cm^{-1} shows the O–H stretching vibration modes of water molecules (Fig. 2e). In dilute solution (1 mol kg^{-1}), the O–H stretching vibration exhibited

the same broad Raman band as the pure water, which is attributed to five hydrogen-bonding environments: DDAA (double donor–double acceptor), DDA (double donor–single acceptor), DAA (single donor–double acceptor), DA (single donor–single acceptor) and free OH in free water clusters[35]. The double proton donor modes (DDAA and DDA) can exist only in the hydrogen-bond network of free water clusters. In $Li_2ZnCl_4{\cdot}9H_2O$, only DAA and enhanced DA peaks are observed, indicating that most of the water was confined in the first solvation shell of Li^+. Different from the 'water-in-bi-salt'[36,37] and highly concentrated $ZnCl_2{\cdot}RH_2O$ electrolytes[12], $Li_2ZnCl_4{\cdot}RH_2O$ can stabilize water even at a low Li^+/H_2O ratio (1/5) or a low cation/H_2O ratio (3/10). The dissociation of $Li^+/ZnCl_4^{2-}$ ion pairs and more sufficient water solvation were also confirmed by the enthalpy change of solution during the mixing of LiCl and $ZnCl_2$ aqueous solutions at a fixed cation/water ratio (Supplementary Fig. 8a). An average energy of 36 joules per mole of water was released when $LiCl{\cdot}3H_2O$ was added to $ZnCl_2{\cdot}3H_2O$ until the Li/Zn ratio reached 2/1 (calculation detail in Methods). As a reference, negligible enthalpy differences were detected in dilute dual-salt solutions and the single-salt aqueous systems. The enthalpy change of mixing results from the redistribution of Cl^- and H_2O associations effectively suppressing $Li^+/ZnCl_4^{2-}$ ion pairing and increasing hydration of Li^+, making the electrolyte more thermodynamically stable with a high entropy.

The rearrangement of the local solvation structure is further studied by examining the activity coefficients of the water and cations. We measured water activity coefficients of $Li_2ZnCl_4{\cdot}RH_2O$ from the vapour-pressure ratio of $Li_2ZnCl_4{\cdot}RH_2O$ solutions to the saturated vapour pressure of pure water at 22 °C (2.69 kPa). Figure 2f shows the dependence of the water activity coefficient on the mole fraction of water in $Li_2ZnCl_4{\cdot}RH_2O$ solutions. These coefficients may be overestimated because the complex salt Li_2ZnCl_4 is treated as two LiCl and one $ZnCl_2$ in the calculation of the water mole fraction. Despite this overestimation, the water in $Li_2ZnCl_4{\cdot}RH_2O$ ($R \leq 9$) exhibited much lower activity coefficients than LiCl–H_2O, $ZnCl_2$–H_2O and 21 m LiTFSI–H_2O, which are normally considered as highly hydrated systems[37–39]. As water molar concentration decreases from 95 mol% to 67 mol%, which equates to a salt concentration increase from 1.0 mol kg^{-1} to 18.5 mol kg^{-1} ($Li_2ZnCl_4{\cdot}6H_2O$), the vapour pressure of water drops from 2.33 kPa to 0.088 kPa, and the water activity coefficient decreases from 0.92 to 0.09 (red line in Fig. 2f) because of a sufficient hydration effect in the Li^+ 'sponge'. The substantially reduced water activity largely serves to suppress the freezing or boiling in $Li_2ZnCl_4{\cdot}RH_2O$ ($R \leq 9$) electrolytes as shown in the thermal analysis in Fig. 1.

The activity coefficients γ of Li^+ and Zn^{2+} in $Li_2ZnCl_4{\cdot}RH_2O$ electrolytes were also estimated by the equilibrium potential of $Li_{0.5}FePO_4$ and Zn metal electrodes, respectively (Fig. 2g; calculation details in Supplementary Information). Remarkably, the γ_{Li} in $Li_2ZnCl_4{\cdot}6H_2O$ are 5×10^5 times higher than that at 1.0 mol kg^{-1}. The large increase in γ has been observed previously in other highly concentrated aqueous solutions[37,40] and is closely related to the changes of electrolyte solvation structure. Such a trend is beyond the scope of conventional Debye–Hückel theory but can be rationalized qualitatively through the Stokes and Robinson hydration effect. The mean ionic activity increases with decreasing water activity. More interestingly, the rate of increase in γ_{Li} for $Li_2ZnCl_4{\cdot}RH_2O$ ($R < 11$) is much larger than that in LiCl solutions, while γ_{Zn} in $Li_2ZnCl_4{\cdot}RH_2O$ increases slower than that in $ZnCl_2$ solutions (Fig. 2g). The large difference in Li/Zn-ion activity between single-ion and dual-ion electrolytes is attributed to reducing the prevalence of Li–Cl ion pairs and Zn–H_2O contacts in $Li_2ZnCl_4{\cdot}RH_2O$ as the dissociated Li–Cl donates Cl^- to Zn^{2+}, thus freeing up water from the Zn^{2+} solvation shell to hydrate Li^+ as observed in MD simulations.

Reversibility of Zn metal anode at various temperatures

The electrochemical performance of the Zn metal anode in $Li_2ZnCl_4{\cdot}9H_2O$ electrolyte and $ZnCl_2{\cdot}3H_2O$ reference electrolyte were evaluated at a current of 0.2 mA cm^{-2} with an aerial capacity of 0.2 mAh cm^{-2} using the Zn||Zn symmetric cells in the temperature range of 80 °C to −70 °C (Fig. 3a). The voltage profiles (a sum of the overpotentials for Zn stripping/plating) of the Zn||Zn cells with both $Li_2ZnCl_4{\cdot}9H_2O$ and $ZnCl_2{\cdot}3H_2O$ electrolytes show excellent stability with a negligible voltage fluctuation during repeated cycling at 20 and 80 °C, similar to most non-alkaline electrolytes[7,8]. However, when the temperature decreases from 20 °C to −70 °C, the overpotential of the Zn||Zn cell with $Li_2ZnCl_4{\cdot}9H_2O$ electrolyte shows only a modest increase from 52 mV at 20 °C to 201 mV at −70 °C. By contrast, the Zn||Zn symmetric cell with $ZnCl_2{\cdot}3H_2O$ electrolyte showed a dramatic polarization increase to >1.8 V at temperatures <−40°C (Fig. 3b) due to a large reduction in conductivities (Fig. 1b) and transference numbers (Supplementary Fig. 2b) at a temperature of −40 °C. With a high current density of 1 mA cm^{-2} or areal capacity of 4 mAh cm^{-2}, the Zn||Zn cell with $Li_2ZnCl_4{\cdot}9H_2O$ electrolyte still shows decent overpotentials across the whole temperature range (Supplementary Fig. 9).

Coulombic efficiency (CE) of Zn plating/stripping in $Li_2ZnCl_4{\cdot}9H_2O$ at various temperatures was further evaluated using Ti||Zn asymmetric cells at a current of 0.4 mA cm^{-2} with a high capacity of 2.0 mAh cm^{-2} (Fig. 3b). An initial CE of 97.50% was achieved at 20 °C. CE increases to ~99.99% after 20 cycles and maintains this high CE for over 100 cycles. The average Zn plating/stripping CE can even reach ~100% at −70 °C due to further reduction in the activity of water. At 80 °C, the CE is still greater than 99.95%. These results reflect the highest measured Zn CEs reported across a wide temperature range for aqueous electrolytes[9]. Similarly high CEs were also achieved at a higher current density of 1 mA cm^{-2} (Supplementary Fig. 10) and different depths of discharge (Supplementary Fig. 11). After 100 cycles, the Zn plated on the Ti substrates still exhibited a dendrite-free morphology (Supplementary Fig. 12). CEs of Zn anode strongly correlated with pH values and the water content (R) in $Li_2ZnCl_4{\cdot}RH_2O$ and $ZnCl_2{\cdot}RH_2O$ electrolytes due to hydrogen evolution. Figure 3c shows the relationship between pH values and CEs of the Zn anode at 20 °C. For $ZnCl_2{\cdot}RH_2O$ electrolytes, even at the highest concentrations (18 mol kg^{-1}), pH remains a somewhat acidic ~4 with a low CE of 95%. By contrast, when the water content is reduced to $R \leq 9$ in $Li_2ZnCl_4{\cdot}RH_2O$, the pH is near neutral and results in a high Zn CE of ~99.99%.

Water reduction potentials depend on the solvate structure as revealed by DFT calculations (Fig. 3d and Supplementary Fig. 8b–h). Water molecules in aqua Zn ions such as $Zn^{2+}(H_2O)_6$ are the most reductively unstable, followed by waters in the hydrated Li^+ solvation shell due to the strong electric fields, which polarize waters in the inner solvation shell. As Dubois et al.[41] and Zhang et al.[10] reported, coordinated waters indeed have higher reduction potentials than free water microscopically in most cases, although both solvates are expected to undergo H_2 evolution reaction at typical overpotentials the electrolyte is experiencing during Zn plating[41]. In Li-based water-in-salt electrolytes, this limitation is addressed through aggregation of Li–TFSI pairs in the super-concentrated regime, which elevates the reduction potential of the anion to be thermodynamically competitive with water reduction[42]. For $ZnCl_2{\cdot}RH_2O$ electrolytes, the limited availability of Cl^- is unable to eliminate the presence of water in the Zn^{2+} coordination shell, and the acidic pH of the electrolyte raises the H_2 evolution reaction potential. By contrast, as water content drops to $R \leq 9$ in $Li_2ZnCl_4{\cdot}RH_2O$, not only is water excluded from Zn^{2+} coordination but the average coordination number of Li^+ and Cl^- increases to at least 1 (Fig. 2c) as $Li^+(H_2O)_3$ tends to share Cl^- ions that are bound to Zn^{2+}. The presence of Cl^- in the Li^+ shell depolarizes the remaining waters in the solvation shell and decreases the H_2 evolution potential, suppressing water decomposition (the neutral pH has a similar effect for free waters). Given the extended electrochemical stability window of $Li_2ZnCl_4{\cdot}RH_2O$ (Supplementary Fig. 13), generation of thick oxide or hydroxide passivation commonly found on a zinc metal anode operated in aqueous electrolytes would be largely suppressed. The absence of a solid electrolyte interphase on the cycled Zn anode in $Li_2ZnCl_4{\cdot}9H_2O$

https://doi.org/10.1038/s41893-022-01028-x

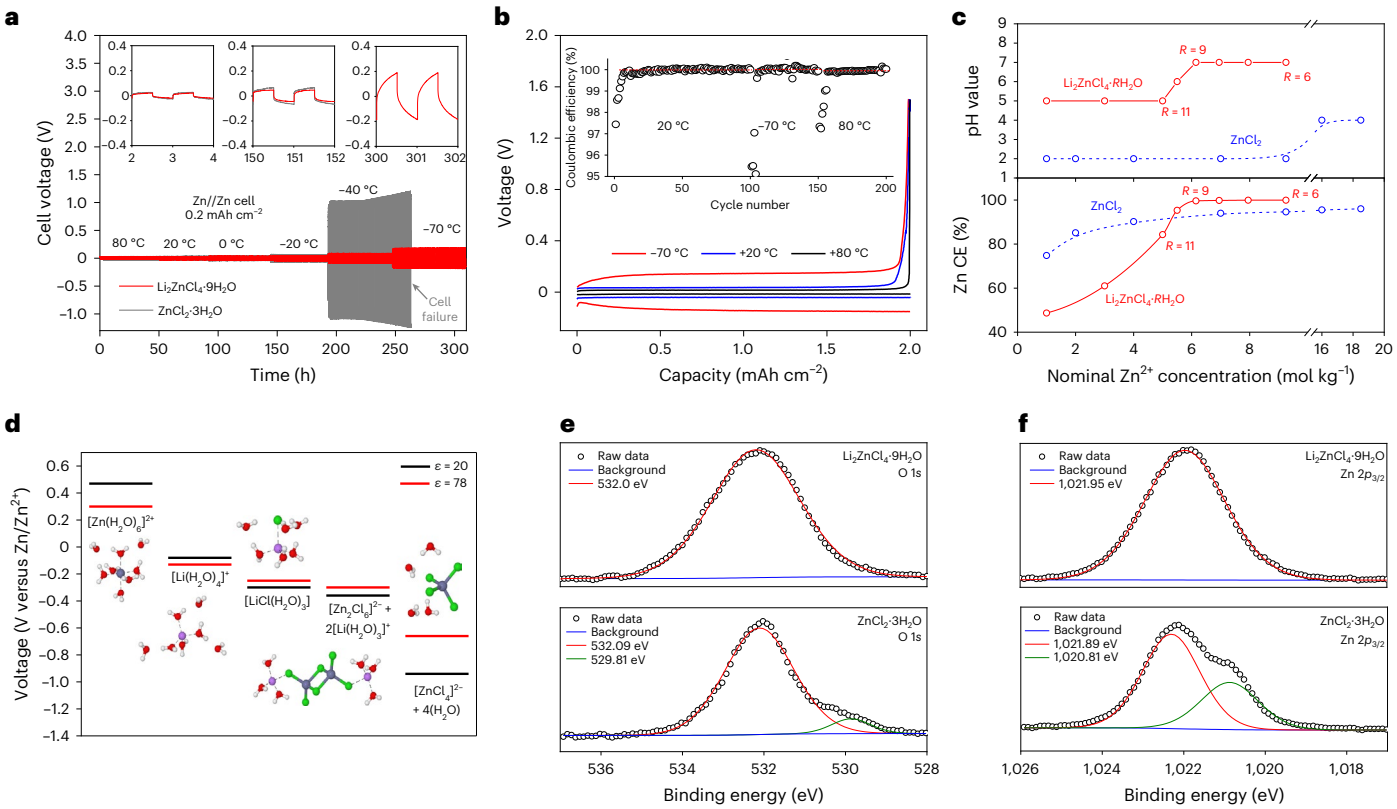

Fig. 3 | Zn metal anode performances. a, Galvanostatic Zn stripping/plating in a Zn||Zn symmetrical cell with $Li_2ZnCl_4{\cdot}9H_2O$ and $ZnCl_2{\cdot}3H_2O$ electrolytes at 0.2 mA cm^{-2} and temperature range from +80 to −70 °C. **b**, The voltage profiles of Zn plating/stripping on a Ti working electrode at 0.4 mA cm^{-2} and temperature range from +80 to −70 °C. Inset shows corresponding CEs of Zn||Ti asymmetrical cell versus cycle number. **c**, The pH values (top) and CEs of Zn plating/strapping (bottom) for $Li_2ZnCl_4{\cdot}RH_2O$ and $ZnCl_2{\cdot}RH_2O$ electrolytes as a function of their water concentrations at 20 °C. **d**, The reduction potentials (versus Zn/Zn^{2+}) for H_2 evolution reactions of different cation–water solvates species predicted by DFT calculations with solvates immersed in implicit solvent with dielectric constants $\varepsilon = 20$ (black) and $\varepsilon = 78$ (red). Jmol colour scheme is used: Li, purple; Zn, grey; Cl, green; O, red; H, white. **e**,**f**, Zn $2p_{3/2}$ (**e**) and O 1*s* (**f**) XPS spectra of Zn anode after the 20th stripping/platting cycle in $Li_2ZnCl_4{\cdot}9H_2O$ and $ZnCl_2{\cdot}3H_2O$ electrolyte.

electrolytes was confirmed by X-ray photoelectron spectroscopy (XPS) characterization. Figure 3e–f show the XPS of the Zn anode surface after the 20th plating/stripping cycle in $Li_2ZnCl_4{\cdot}9H_2O$ and $ZnCl_2{\cdot}3H_2O$ electrolytes. No ZnO or $Zn(OH)_2$ was detected in $2p_{3/2}$ core level of Zn anode surface cycled in $Li_2ZnCl_4{\cdot}9H_2O$ electrolyte. By contrast, an extra fitting peak at 1,020.81 eV attributed to ZnO (Zn^{II}) was found even in highly concentrated $ZnCl_2{\cdot}3H_2O$[43,44]. Meanwhile, the Gaussian–Lorentzian peak with a binding energy of 529.81 eV can be ascribed to O^{2-} ions in the wurtzite structure of ZnO[45,46]. The other peak located at 532.09 eV was assigned to the presence of C=O bonding originating from surface adsorbed organic residues. Therefore, ZnO was formed on cycled Zn anode in $ZnCl_2{\cdot}3H_2O$ electrolyte but was absent on cycled Zn in $Li_2ZnCl_4{\cdot}9H_2O$ electrolytes.

Zn–air battery enabled by HEE

Zn–air pouch cells using platinum–carbon catalyst (5% Pt loading) coated porous carbon as an air cathode and commercial porous Zn metal as an anode were assembled to demonstrate the unprecedented thermal stability of $Li_2ZnCl_4{\cdot}9H_2O$ electrolyte between 80 °C and −60 °C (Fig. 4). Figure 4a shows 10 h charge/discharge profiles at a specific current of 0.4 mA cm^{-2} with a discharge potential of 1.07 V and a charge potential of 1.76 V at 20 °C. Notably, the average discharge potentials shifted to 0.84 V and 0.67 V only after the temperature dropped to −40 °C and −60 °C, respectively. The Zn–air cell operated stably in ambient air for 700 h at both 20 °C and −60 °C with a 10 h charge and discharge duration time per cycle (Fig. 4b). Besides the excellent ionic conductivity retention, the uniqueness of $Li_2ZnCl_4{\cdot}9H_2O$ electrolyte also converts the cathode reaction from the $4e^-/O_2$ pathway ($O_2 + 2H_2O + 4e^- \leftrightarrow 4OH^-$) into a more facile $2e^-/O_2$ pathway ($Zn^{2+} + O_2 + 2e^- \leftrightarrow ZnO_2$) to guarantee the fast kinetics at low temperature. By contrast, all the commercial batteries fail to cycle properly because of a high cell impedance below −20 °C at the C/10 rate (Supplementary Fig. 14). Since the vapour pressure of water for $Li_2ZnCl_4{\cdot}9H_2O$ electrolyte was only 350 Pa, the water evaporation in an open atmosphere was negligible, ensuring a long-term practical operation.

The formation of ZnO_2 on air cathode through $2e^-/O_2$ reaction ($Zn^{2+} + O_2 + 2e^- \leftrightarrow ZnO_2$) was confirmed by scanning electron microscope (SEM), energy-dispersive X-ray (EDX) and X-ray diffraction (XRD). Figure 4c shows SEM images of air cathodes obtained after the tenth discharge. The discharge reaction product had a disk-like morphology with a diameter of 1–2 μm (upper-left part) on top of chuncky carbon black particles. EDX mapping showed the corresponding distribution of Zn and O elements in this reaction product and no Cl distribution, excluding the possibility of forming zinc chloride hydroxide monohydrate ($Zn_5(OH)_8Cl_2{\cdot}H_2O$). To further identify the discharge products, air cathodes were examined by XRD (Fig. 4d), showing only obvious patterns of ZnO_2 and carbon black. MD simulations predicted that the $ZnCl_4^{2-}$-based aggregates remain intact in the electric double layer. The $ZnCl_4^{2-}$ species are attracted towards the air cathode surface (carbon) under a positive polarization, while water near $ZnCl_4^{2-}$ was bound to Li^+, making it more oxidatively stable (Fig. 4e and Supplementary Fig. 15). The Zn ion was much closer to the electrode surface (~4.3 Å) in $Li_2ZnCl_4{\cdot}9H_2O$ than in regular electrolytes with one layer of Cl^- in between[47], which indicated a facile reaction route between

https://doi.org/10.1038/s41893-022-01028-x

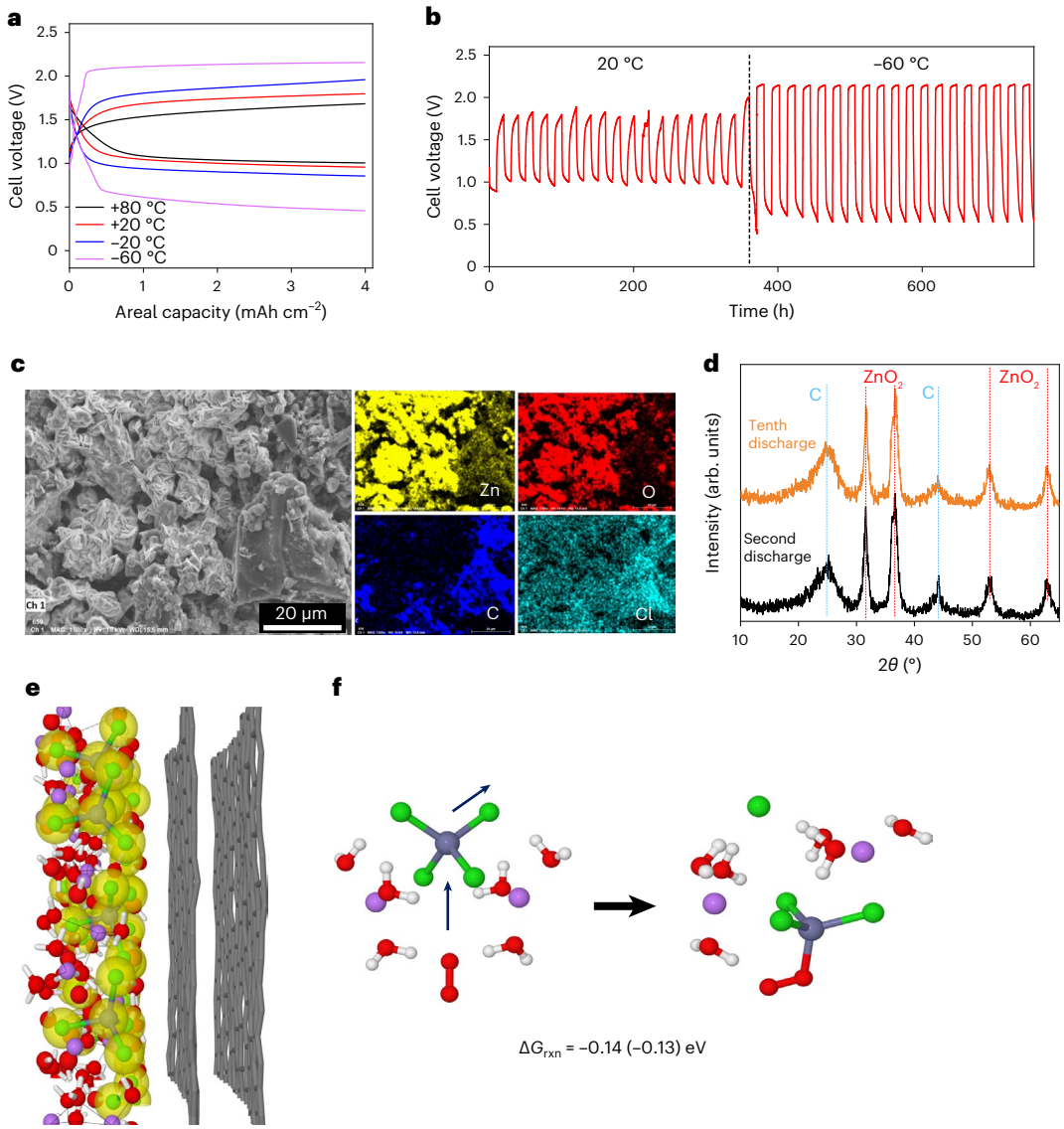

Fig. 4 | Zn–air cell performances. a, Galvanostatic voltage profiles in a capacity-fixed mode (fixed capacity: 8.0 mAh cm^{-2}) of the Zn–air pouch cell with $Li_2ZnCl_4{\cdot}9H_2O$ electrolyte at the temperature range between 80 °C and −60 °C with a specific current of 0.4 mA cm^{-2} and a fixed capacity of 4.0 mAh cm^{-2}. **b**, Long-term cycling performance (800 h) of Zn–air cells at 20 °C and −60 °C at a specific current of 0.4 mA cm^{-2}. **c**, SEM images (left) and corresponding EDX mapping (Zn, O, C and Cl, right) of air cathodes obtained after tenth discharge. **d**, Corresponding XRD patterns of air cathodes obtained after discharge and charge after second and tenth discharges. **e**, Schematic snapshots (side view) of the interfacial structures at the air cathodes with positive polarization applied (charge density q = +0.0128 e$^-$ carbon^{-1}) with the yellow isosurface highlighting $[ZnCl_{4-m}{}^{2-m}]_n$ anions ($n \leq 3$). Jmol colour scheme is used. The dark grey wireframe is the carbon electrode. **f**, Free energy change from M05-2X/6-311++G(3df,3pd) calculation with polarizable continuum models (PCM) of acetone and water (with the value in water in parentheses) implicit solvation model for the reaction of hydrated Li_2ZnCl_4 replacing one Cl^- with O_2^-.

Zn ion and peroxide. In terms of reaction free energy (Fig. 4f), there is a minor preference of −0.14 eV (ε = 20) and −0.13 (ε = 78) for O_2^- to replace a Cl^-, which made it favourable to advance the $2e^-/O_2$ pathway ($Zn^{2+} + O_2 + 2e^- \leftrightarrow ZnO_2$). The smaller preference compared with a $Zn(OTf)_2$ electrolyte also enhances the reversibility of this reaction in $Li_2ZnCl_4{\cdot}9H_2O$ electrolyte. Just as in the Zn||Ti closed cells, no passivation layer (oxides or hydroxides) was found on the Zn metallic anode in these open Zn–air cells (Supplementary Fig. 16).

In addition to the Zn–air battery, $Zn||Zn_xVOPO_4{\cdot}2H_2O$ zinc-ion batteries also demonstrated unprecedented performance in $Li_2ZnCl_4{\cdot}9H_2O$ electrolytes over a wide temperature range (Supplementary Fig. 17). At −70 °C and −80 °C, the $Li_2ZnCl_4{\cdot}9H_2O$ electrolyte still provided a 90.0% and 81.1% discharge capacity retention relative to 20 °C, respectively, which is superior to the other reported low-temperature rechargeable batteries (Supplementary Video 1)[16,17,48,49].

Discussion

In summary, a high-entropy electrolyte concept was demonstrated using a $Li_2ZnCl_4{\cdot}9H_2O$ electrolyte. The competition between Li–Cl dissociation, reduction in the length of $[ZnC_{4-m}{}^{2-m}]_n$ aggregates and disruption of the free solvent hydrogen-bond network produces a unique frustrated solvation structure with a high entropy that helps to retain excellent ionic conductivities where the solvent is greatly stabilized and crystallization is suppressed. Thus, both a wide electrochemical stability window (better than water-in-salt electrolytes) and an exceptional operating temperature range (−80 °C to +80 °C, found only in this electrolyte) were achieved simultaneously. Through our extensive characterization efforts, the demonstrated relationships among the solvation structure, transport and electrochemical stability of the electrolyte provide a basis of understanding that inspires the future design of electrolytes for aqueous metal-ion batteries.

As a demonstration of the efficacy of the high-entropy solvation environment concept, unprecedented stability of a Zn–air battery was achieved across a temperature range of −60 °C to 20 °C. Despite the wide use of chloride-containing electrolytes in commercial primary batteries (for example, zinc–manganese dioxide battery, Zn–carbon battery, lithium–thionyl chloride battery) and proposed in rechargeable multivalent ion batteries (for example, zinc-ion, magnesium-ion, aluminium-ion), corrosion issues may need to be addressed by anti-corrosion coating, inhibitors or carbonized current collectors for future applications.

Methods

Preparation of materials and electrolytes

All the chloride salts aqueous electrolytes were prepared by dissolving various molar ratios of anhydrous lithium chloride (LiCl; ≥99%; Sigma-Aldrich) and anhydrous zinc chloride ($ZnCl_2$; ≥99%; Sigma-Aldrich) in water (high-performance liquid chromatography grade). $VOPO_4{\cdot}2H_2O$ powder was synthesized by mixing 4.8 g of V_2O_5 powder (≥98%; Sigma-Aldrich) in 26.6 ml 85% H_3PO_4 (ACS reagent, ≥85 wt% in H_2O; Sigma-Aldrich) and 115.4 ml distilled water. The mixture was refluxed at 110 °C for 16 h. The yellow-green $VOPO_4{\cdot}2H_2O$ powder was filtered, washed with acetone two times and dried under ambient conditions. Zn pre-intercalated compound, $Zn_xVOPO_4{\cdot}2H_2O$, was prepared by reaction at ambient temperature of as-prepared $VOPO_4{\cdot}2H_2O$ powder with stoichiometric amounts of a 0.5 mM solution of zinc iodide (≥99%; Sigma-Aldrich) in distilled water with magnetic stirring for 12 h; after standing for 24 h in an open environment, the target product was collected. The reaction is illustrated as follows:[50]

$$VOPO_4 \cdot 2H_2O + xZnI_2 \overset{H_2O}{\rightarrow} Zn_xVOPO_4 \cdot 2H_2O + I_2$$

Electrochemical measurements

The ionic conductivity measurements were conducted using home-made two Ti disk (Sigma-Aldrich) electrode cells calibrated by 0.1 mol l^{-1} NaCl standard electrolyte (Sigma-Aldrich). The four-point electrochemical impedance spectroscopy (EIS) measurements were performed with Gamry 345 interface 1000 using 5 mV perturbation with the frequency range of 0.01 Hz to 100,000 Hz in an environmental test chamber (Thermal Product Solutions). The air cathode for Zn–air batteries was prepared by doctor-blade coating the slurry of 5% platinum loaded carbon black (XC-72, Fuel Cell Store; 90 wt%), polyvinylidene fluoride (10 wt%; Sigma-Aldrich) and n-methyl-2-pyrrolidone (Sigma-Aldrich) on carbon paper (thickness: 215 µm; Fuel Cell Store). The areal loading of catalysts was ~11 mg cm^{-2}. $VOPO_4{\cdot}2H_2O$ cathode Zn-ion batteries were fabricated by compressing well-mixed active materials, carbon black (Sigma-Aldrich) and poly(vinylidenedifluoride) (Sigma-Aldrich) at a weight ratio of 70/20/10 on a titanium metal mesh (Alfa Aesar, 100 mesh). The areal loading of cathode material was ~18 mg cm^{-2}. Zn||Zn and Ti||Zn cells were assembled as CR2032-type coin cells using Zn metal disk (Alfa Aesar, 2 cm^2) and glass fibre (VWR) as a separator. $VOPO_4{\cdot}2H_2O$||Zn and Zn–O_2 pouch cells (2 cm × 4 cm) were assembled using $VOPO_4{\cdot}2H_2O$ or air cathodes, commercial metallic zinc anodes and glass fibre as separator, respectively. Zn–air pouch cells were cut open on the cathode side. These cells were then galvanostatically charged/discharged using a Land BT2000 battery test system in an environmental test chamber (Thermal Product Solutions). To separate the Li-ion conduction contribution from the Zn-ion transport in this high entropy system, the transference number t_{Zn}, defined as the net ratio of faradays of charge carried by the Zn constituent, was examined by the steady-state current method in a Zn||Zn symmetric cell[41]. Since the CE of Zn stripping/plating was close to 100% in $Li_2ZnCl_4{\cdot}RH_2O$ ($R \geq 9$), t_{Zn} could be estimated by the following equation

$$t_{Zn} = \frac{I_S(\Delta V - I_0R_0)}{I_0(\Delta V - I_SR_S)}$$

where I_S and I_0 are the steady-state and initial currents, respectively, when 5 mV of polarization voltages ΔV are applied across the cell (Supplementary Fig. 2c). The first data point was recorded at 0.05 s. R_0 and R_S are the initial and steady-state resistances measured by EIS to balance the potential change of interface resistance.

Raman spectroscopy

For the solution structure measurements, Raman spectra were collected with a Horiba Jobin Yvon Labram Aramis Raman spectrometer using a laser (wavelength of 532 nm) at frequencies between 3,500 cm^{-1} and 60 cm^{-1}. Six spectra per sample were collected and integrated to get a high signal/noise ratio.

Differential scanning calorimetry

Phase and glass transitions were conducted at a slow heating rate of 2 °C min^{-1} using two differential scanning calorimeters (DSC250 or MDSC 2920, both by TA Instruments). A liquid nitrogen cooler was used for low-temperature control, and calibration was performed using the standards of cyclohexane (−87.06 °C for a solid-solid transition and 6.45 °C for melting), indium (156.60 °C for melting) and tin (231.93 °C for melting). For DSC samples, about 10 mg of electrolyte liquid was enclosed in an aluminium pan and lid (0219–0062, PerkinElmer Instruments) and hermetically sealed with a crimper (0219–0061, PerkinElmer). Vitrification of a sample was achieved by predipping the sample into liquid nitrogen and subsequently scanning it up through its glass transition. Crystallization of a sample that was otherwise hard to crystalize was assisted by adding a small amount of mesocarbon microbeads (MTI Corporation) into the DSC sample as a nucleating agent to induce the desired crystallization.

MD simulations

Polarizable force-field simulations were performed with an in-house modified version of the Tinker-HP v.1.0 package and a locally modified AMOEBA-BIO 2018 force field[51,52]. Initial configurations for simulations were generated with Materials Studio's amorphous cell-packing utility at a density of 1 g ml^{-1}; in all cases the density increases after volume relaxation[53]. We reduced ion charges by 2.5% and refit the Cl–OH_2 (3.925 Å, 0.32 kcal mol^{-1}), Li–Cl (3.7011 Å, 0.1451 kcal mol^{-1}) and Zn–Cl (3.48 Å, 0.28 kcal mol^{-1}) van der Waals terms. Scaling the charges slightly had a relatively large impact on the transport properties and improved agreement with experimental values. As a multitude of simulations with varying size and composition were prepared, we conserve as many of the settings between simulations as possible: in the constant number, constant pressure, and constant temperature (NPT) ensemble, all simulations are thermostated at 298.15 K unless noted otherwise and barostated at 1 atm using the Berendsen method with a 1.0 femtosecond (fs) integration time step using the Beeman integrator[54], while all simulations in the constant number, constant volume, and constant temperature (NVT) ensemble employed Berendsen thermostating at 298.15 K unless noted otherwise and the reference system propagator algorithm integrator with a 2.0 fs time step[55]. Non-bonded terms use a uniform cut-off of 10 Å if the box length is >20 Å. A long-range correction is always applied to van der Waals interactions. Particle mesh Ewald is used for electrostatics with a fixed alpha of 0.386 $Å^{-1}$ and a conservative grid of 60^3 points (>1 point per $Å^3$) for $ZnCl_2$–RH_2O (R = 4, 6, 8–11, 13, 15, 17) and Li_2ZnCl_4–RH_2O (R = 4, 6, 8–11, 13, 15, 17) simulations with ~2,200 waters each and LiCl–$3H_2O$ with 4,608 waters. A grid of 48^3 points is used for LiCl–RH_2O (R = 3,4) simulations, each with 1,152 waters. The LiCl–RH_2O simulations from the initial geometry were evolved for 6 ns in the NPT ensemble, then the final configuration was resized to match the average box size from the final 2 ns. The $ZnCl_2$–RH_2O and Li_2ZnCl_4–RH_2O simulations evolved for 16 ns from the initial geometry in the NPT ensemble, with the final snapshots for each composition resized to match the average box size from the final 4 ns of the trajectory. All of these simulations were run for

24 ns in the NVT ensemble with the resized box and used for analysis. Coordinates were saved at a 2 ps frequency and the pressure stress tensor at an interval of 10 fs.

Two sets of trajectories were prepared for BOMD. The first set comprises smaller cells of $Li_2ZnCl_4{\cdot}RH_2O$ (R = 6, 15) electrolytes that were prepared just as the larger cells but using higher temperatures as discussed in Supplementary Information. An initial set of four replicas was prepared. Equilibration under constant pressure conditions was performed for 6 ns, with the average box size taken from the last 2 ns. The final frame was rescaled to this average box size before 8 ns of constant volume dynamics was performed. Using the same box volume to create a different trajectory, a small 2% increase in the Zn–Cl repulsion term was added to slightly alter the solvation shell around the Zn. The effect was more pronounced on the 15/1 system than the 6/1 system, where little change in solvation structure was observed. The non-bonded cut-offs were set to at least 7.0 Å, but we used 8.0 Å where it was possible and a 24^3 particle mesh Ewald grid. This set of trajectories was modelled with the PBE-D3 functional in BOMD. A second set of trajectories was added later for R = 6, 9, 10 and 15 in $Li_2ZnCl_4{\cdot}RH_2O$; they were set up and run the same way as the first set but with 0% Zn–Cl repulsion scaling and 5% and 7.5% scaling to sample very different initial Zn coordination environments. This second set of trajectories was modelled with PBE-D3 and revPBE-D3 in BOMD.

The final structures from the smaller cell NVT runs were then used as inputs for BOMD simulations. BOMD calculations were performed with CP2K v.6.1 at the [PBE-D3 or revPBE-D3]/DZVP-MOLOPT-SR-GTH level of theory with PBE optimized pseudopotentials for core states using a 600 Ry cut-off[56–63]. Trajectories were heated in 100 K increments to their respective target temperatures (discussed in Supplementary Information) using the Bussi velocity rescaling thermostat under constant volume conditions with 20 fs coupling constant[64]. Total annealing time was 10 ps using a 0.5 fs time step throughout. Up to 145 ps of isotropic constant pressure dynamics was performed starting from the thermalized NVT configurations, with 50 fs coupling constant for the Bussi thermostat[65]. The first 10 ps is discarded as additional equilibration and changes in the coordination number around Zn are monitored after that. The bias that excludes Zn–Cl ion pairing in FF-MD is not present in BOMD; we monitor for convergence in the coordination numbers across all three replicates per composition over time.

Activity coefficient measurements

To study the activity of Li^+ and Zn^{2+} as a function of the Li^+ molality, the equilibrium potentials of the Li_xFePO_4 (x = 0.5) electrode and Zn metal electrode in various electrolyte solutions were measured using a two-electrode cell with an Ag/AgCl (in saturated KCl aqueous solution) reference electrode, respectively. Water activity measurements were performed using a custom-built vapour-pressure measurement apparatus. Solutions were placed in a glass container, which had a sample/headspace ratio of approximately 1/1, that was connected to a vacuum system. For purging and degassing, the glass chamber was evacuated using a vacuum pump to P < 0.1 kPa and flushed three times with nitrogen. The volume and mass of the solution were measured in control experiments to ensure that the amount of sample loss during purging was negligible. After purging, the chamber was sealed, and the total pressure was monitored as a function of time as the vapour phase equilibrated with the solution phase. When the total pressure reached a constant value, the pressure was recorded. A k-type thermocouple was inserted into the liquid mixture to ensure the temperature was 22 °C before recording the pressure. It was assumed that the vapour phase was pure water (no salt evaporation). Control experiments were conducted with pure milli-Q water, and the tabulated saturated vapour pressure of 2.69 kPa was accurately measured. Raoult's law was used to calculate the water activity in the liquid phase from the measured water-vapour pressure.

Neutron and X-ray scattering

SANS measurements were performed on the very small-angle neutron scattering (vSANS) instrument at the National Institute of Standards and Technology Center for Neutron Research. Samples were contained in 1 mm path standard titanium demountable cells using titanium windows. A closed-cycle refrigerator was employed for controlling the sample temperature with an accuracy better than 1 K. Data were collected using two incoming neutron wavelengths of 5 Å and 8.5 Å with $\Delta\lambda/\lambda \approx 0.13$. With the combined use of two detector banks, a Q range from ~10^{-3} $Å^{-1}$ to ~0.2 $Å^{-1}$ was covered. Employing standard routines[66], raw data were corrected for background and empty cell scattering and further reduced to one-dimensional (1D) absolute intensity patterns using open-beam intensity.

X-ray scattering spectra of aqueous solutions were collected with beamline 11-ID-C at the Advanced Photon Source at Argonne National Laboratory with light wavelength of 0.11729 Å. Samples with an average volume of ~0.2 ml were held in a 3 mm quartz tube, while 2D diffraction images were collected on a GE amorphous silicon-based detector. All the preceding data were acquired at 300 K. Pair distribution functions–$G(r)$ were computed using GSAS II software. Scattering from an empty quartz tube was used for background subtraction. Corrections for fluorescence, X-ray polarization, Compton scattering and energy dependence were then applied.

Data availability

The datasets generated and/or analysed during the current study are available from the corresponding authors on reasonable request.

References

1. Grey, C. & Tarascon, J. Sustainability and in situ monitoring in battery development. *Nat. Mater.* **16**, 45–56 (2017).
2. Newton, G. N., Johnson, L. R., Walsh, D. A., Hwang, B. J. & Han, H. Sustainability of battery technologies: today and tomorrow. *ACS Sustain. Chem. Eng.* **9**, 6507–6509 (2021).
3. Suo, L. et al. 'Water-in-salt' electrolyte enables high-voltage aqueous lithium-ion chemistries. *Science* **350**, 938–943 (2015).
4. Suo, L. et al. How solid–electrolyte interphase forms in aqueous electrolytes. *J. Am. Chem. Soc.* **139**, 18670–18680 (2017).
5. Yang, C. et al. Unique aqueous Li-ion/sulfur chemistry with high energy density and reversibility. *Proc. Natl Acad. Sci. USA* **114**, 6197–6202 (2017).
6. Yang, C. et al. Aqueous Li-ion battery enabled by halogen conversion–intercalation chemistry in graphite. *Nature* **569**, 245–250 (2019).
7. Cao, L. et al. Fluorinated interphase enables reversible aqueous zinc battery chemistries. *Nat. Nanotechnol.* **16**, 902–910 (2021).
8. Zhang, C. et al. A $ZnCl_2$ water-in-salt electrolyte for a reversible Zn metal anode. *Chem. Commun.* **54**, 14097–14099 (2018).
9. Wang, F. et al. Highly reversible zinc metal anode for aqueous batteries. *Nat. Mater.* **17**, 543–549 (2018).
10. Zhang, Q. et al. Designing anion-type water-free Zn^{2+} solvation structure for robust Zn metal anode. *Angew. Chem. Int. Ed.* **60**, 23357–23364 (2021).
11. Zhu, Y. et al. Concentrated dual-cation electrolyte strategy for aqueous zinc-ion batteries. *Energy Environ. Sci.* **14**, 4463–4473 (2021).
12. Zhang, Q. et al. Modulating electrolyte structure for ultralow temperature aqueous zinc batteries. *Nat. Commun.* **11**, 4463 (2020).
13. Angell, C. A., Ngai, K. L., McKenna, G. B., McMillan, P. F. & Martin, S. W. Relaxation in glassforming liquids and amorphous solids. *J. Appl. Phys.* **88**, 3113–3157 (2000).
14. Rodrigues, M.-T. F. et al. A materials perspective on Li-ion batteries at extreme temperatures. *Nat. Energy* **2**, 17108 (2017).
15. Scherer, G. W. Editorial comments on a paper by Gordon S. Fulcher. *J. Am. Chem. Soc.* **75**, 1060–1062 (1992).

16. Fan, X. et al. All-temperature batteries enabled by fluorinated electrolytes with non-polar solvents. *Nat. Energy* **4**, 882–890 (2019).
17. Dong, X. et al. High-energy rechargeable metallic lithium battery at −70 °C enabled by a cosolvent electrolyte. *Angew. Chem. Int. Ed.* **58**, 5623–5627 (2019).
18. Borodin, O. et al. Liquid structure with nano-heterogeneity promotes cationic transport in concentrated electrolytes. *ACS Nano* **11**, 10462–10471 (2017).
19. Horne, R. The adsorption of zinc(II) on anion-exchange resins. I. The secondary cation effect. *J. Phys. Chem.* **61**, 1651–1655 (1957).
20. Kraus, C. A. The ion-pair concept, its evolution and some applications. *J. Phys. Chem.* **60**, 129–141 (1956).
21. Sosso, G. C. et al. Crystal nucleation in liquids: open questions and future challenges in molecular dynamics simulations. *Chem. Rev.* **116**, 7078–7116 (2016).
22. Gu, G. Y. et al. 2-Methoxyethyl (methyl) carbonate-based electrolytes for Li-ion batteries. *Electrochim. Acta* **45**, 3127–3139 (2000).
23. Angell, C. A. Liquid fragility and the glass transition in water and aqueous solutions. *Chem. Rev.* **102**, 2627–2650 (2002).
24. Wilcox, R. J. et al. Crystalline and liquid structure of zinc chloride trihydrate: a unique ionic liquid. *Inorg. Chem.* **54**, 1109–1119 (2015).
25. Wood, B. C. et al. Paradigms of frustration in superionic solid electrolytes. *Phil. Trans. R. Soc. A* **379**, 20190467 (2021).
26. Brehler, B. & Jacobi, H. Die Kristallstruktur des $Li_2ZnCl_4{\cdot}2H_2O$. *Naturwissenschaften* **51**, 11 (1964).
27. Xu, W., Cooper, E. I. & Angell, C. A. Ionic liquids: ion mobilities, glass temperatures, and fragilities. *J. Phys. Chem. B* **107**, 6170–6178 (2003).
28. Marcus, Y. & Hefter, G. Ion pairing. *Chem. Rev.* **106**, 4585–4621 (2006).
29. Ansell, S., Dupuy-Philon, J., Jal, J. & Neilson, G. Ionic structure in the aqueous electrolyte glass. *J. Phys. Condens. Matter* **9**, 8835 (1997).
30. Quicksall, C. O. & Spiro, T. G. Raman spectra of tetrahalozincates and the structure of aqueous $ZnCl_4$. *Inorg. Chem.* **5**, 2232–2233 (1966).
31. Irish, D. E., McCarroll, B. & Young, T. F. Raman study of zinc chloride solutions. *J. Chem. Phys.* **39**, 3436–3444 (1963).
32. Kajinami, A., Kubota, M., Mizuhata, M. & Shigehito, D. The variaiton of structure with composition for mixed molten hydrate. *Molten Salts VII: Proc. of the International Symposium* (ed. Trulove, P. C.) 263–274 (ECS, 2000).
33. Maeda, M., Ito, T., Hori, M. & Johansson, G. The structure of zinc chloride complexes in aqueous solution. *Z. Naturforsch. A* **51**, 63–70 (1996).
34. Yamaguchi, T., Hayashi, S. & Ohtaki, H. X-ray diffraction and Raman studies of zinc(II) chloride hydrate melts, $ZnCl_2{\cdot}rH_2O$ (r=1.8, 2.5, 3.0, 4.0, and 6.2). *J. Phys. Chem.* **93**, 2620–2625 (1989).
35. Sun, Q. The Raman OH stretching bands of liquid water. *Vib. Spectrosc.* **51**, 213–217 (2009).
36. Zhang, J. et al. 'Water-in-salt' polymer electrolyte for Li-ion batteries. *Energy Environ. Sci.* **13**, 2878–2887 (2020).
37. Yamada, Y. et al. Hydrate-melt electrolytes for high-energy-density aqueous batteries. *Nat. Energy* **1**, 16129 (2016).
38. Robinson, R. A. The water activities of lithium chloride solutions up to high concentrations at 25°. *Trans. Faraday Soc.* **41**, 756–758 (1945).
39. Gislason, E. A. Thermodynamics and chemistry (DeVoe, Howard). *J. Chem. Educ.* **78**, 1186 (2001).
40. Stokes, R. H. & Robinson, R. A. Ionic hydration and activity in electrolyte solutions. *J. Am. Chem. Soc.* **70**, 1870–1878 (1948).
41. Dubouis, N. et al. The fate of water at the electrochemical interfaces: electrochemical behavior of free water versus coordinating water. *J. Phys. Chem. Lett.* **9**, 6683–6688 (2018).
42. Hou, X. et al. 'Water-in-Eutectogel' electrolytes for quasi-solid-state aqueous lithium-ion batteries. *Adv. Energy Mater.* **12**, 2200401 (2022).
43. Biesinger, M. C., Lau, L. W., Gerson, A. R. & Smart, R. S. C. Resolving surface chemical states in XPS analysis of first row transition metals, oxides and hydroxides: Sc, Ti, V, Cu and Zn. *Appl. Surf. Sci.* **257**, 887–898 (2010).
44. Tay, Y., Li, S., Sun, C. & Chen, P. Size dependence of Zn 2p 3⁄2 binding energy in nanocrystalline ZnO. *Appl. Phys. Lett.* **88**, 173118 (2006).
45. Das, J. et al. Micro-Raman and XPS studies of pure ZnO ceramics. *Phys. B* **405**, 2492–2497 (2010).
46. Al-Gaashani, R., Radiman, S., Daud, A., Tabet, N. & Al-Douri, Y. XPS and optical studies of different morphologies of ZnO nanostructures prepared by microwave methods. *Ceram. Int.* **39**, 2283–2292 (2013).
47. Sun, W. et al. A rechargeable zinc–air battery based on zinc peroxide chemistry. *Science* **371**, 46–51 (2021).
48. Rustomji, C. S. et al. Liquefied gas electrolytes for electrochemical energy storage devices. *Science* **356**, eaal4263 (2017).
49. Dong, X., Guo, Z., Guo, Z., Wang, Y. & Xia, Y. Organic batteries operated at −70 °C. *Joule* **2**, 902–913 (2018).
50. Jacobson, A., Johnson, J. W., Brody, J., Scanlon, J. & Lewandowski, J. Redox intercalation reactions of vanadium oxide phosphate dihydrate ($VOPO_4{\cdot}2H_2O$) with mono- and divalent cations. *Inorg. Chem.* **24**, 1782–1787 (1985).
51. Lagardère, L. et al. Tinker-HP: a massively parallel molecular dynamics package for multiscale simulations of large complex systems with advanced point dipole polarizable force fields. *Chem. Sci.* **9**, 956–972 (2018).
52. Ren, P. & Ponder, J. W. Polarizable atomic multipole water model for molecular mechanics simulation. *J. Chem. Phys. B* **107**, 5933–5947 (2003).
53. Biovia, D. S. Materials Studio Modeling Environment 4 (Dassault Systèmes, 2015).
54. Berendsen, H. J., Postma, J. V., Van Gunsteren, W. F., DiNola, A. & Haak, J. R. Molecular dynamics with coupling to an external bath. *J. Chem. Phys.* **81**, 3684–3690 (1984).
55. Tuckerman, M., Berne, B. J. & Martyna, G. J. Reversible multiple time scale molecular dynamics. *J. Chem. Phys.* **97**, 1990–2001 (1992).
56. Hutter, J., Iannuzzi, M., Schiffmann, F. & VandeVondele, J. cp2k: atomistic simulations of condensed matter systems. *Wiley Interdiscip. Rev. Comput. Mol. Sci.* **4**, 15–25 (2014).
57. Perdew, J. P., Burke, K. & Ernzerhof, M. Generalized gradient approximation made simple. *Phys. Rev. Lett.* **77**, 3865 (1996).
58. Grimme, S., Antony, J., Ehrlich, S. & Krieg, H. A consistent and accurate ab initio parametrization of density functional dispersion correction (DFT-D) for the 94 elements H–Pu. *J. Chem. Phys.* **132**, 154104 (2010).
59. Grimme, S., Ehrlich, S. & Goerigk, L. Effect of the damping function in dispersion corrected density functional theory. *J. Comput. Chem.* **32**, 1456–1465 (2011).
60. Goedecker, S., Teter, M. & Hutter, J. Separable dual-space Gaussian pseudopotentials. *Phys. Rev. B* **54**, 1703 (1996).
61. Hartwigsen, C., Gœdecker, S. & Hutter, J. Relativistic separable dual-space Gaussian pseudopotentials from H to Rn. *Phys. Rev. B* **58**, 3641 (1998).
62. VandeVondele, J. et al. Quickstep: fast and accurate density functional calculations using a mixed Gaussian and plane waves approach. *Comput. Phys. Commun.* **167**, 103–128 (2005).
63. VandeVondele, J. & Hutter, J. Gaussian basis sets for accurate calculations on molecular systems in gas and condensed phases. *J. Chem. Phys.* **127**, 114105 (2007).

64. Bussi, G., Donadio, D. & Parrinello, M. Canonical sampling through velocity rescaling. *J. Chem. Phys.* **126**, 014101 (2007).
65. Martyna, G. J., Tuckerman, M. E., Tobias, D. J. & Klein, M. L. Explicit reversible integrators for extended systems dynamics. *Mol. Phys.* **87**, 1117–1157 (1996).
66. Kline, S. R. Reduction and analysis of SANS and USANS data using IGOR Pro. *J. Appl. Crystallogr.* **39**, 895–900 (2006).

Acknowledgements

We thank A. Angell at Arizona State University for invaluable advice. We also thank K. Gaskell from Department of Chemistry and Biochemistry at University of Maryland and I. Hill from Department of Physics and Atmospheric Science at Dalhousie University for the guidance of XPS analysis. The principal investigator (C.W.) received financial support from the US Department of Energy (DOE) through ARPA-E grant DEAR0000389. O.B., J.V. and T.P.P. acknowledge support from the US Army, DEVCOM Army Research Laboratory and the Joint Center for Energy Storage Research (JCESR) funded by the Department of Energy, through IAA SN2020957. C.Y. acknowledges the support of the Natural Sciences and Engineering Research Council of Canada (NSERC) through Discovery Grant RGPIN-2021-02426. J.-P. Piquemal and L. Lagardere (Sorbonne Université) helped with Tinker-HP installation and modification. E.T. and A.K. acknowledge financial support from the National Science Foundation through grant CBET 1847469. E.H. and X.-Q.Y. are supported by the Assistant Secretary for Energy Efficiency and Renewable Energy, Vehicle Technology Office of the US DOE through the Advanced Battery Materials Research (BMR) Program. Access to the vSANS instrument was provided by the Center for High Resolution Neutron Scattering, a partnership between the National Science Foundation and the National Institute of Standards and Technology under agreement DMR-1508249. This research used resources 7-BM (QAS) of the National Synchrotron Light Source II, a US DOE Office of Science user facility operated for the DOE Office of Science by Brookhaven National Laboratory under contract no. DE-SC0012704. Certain commercial equipment, instruments, materials, suppliers or software are identified in this paper to foster understanding. Such identification does not imply recommendation or endorsement by the National Institute of Standards and Technology, nor does it imply that the materials or equipment identified is necessarily the best available for the purpose.

Author contributions

C.Y., O.B. and C.W. conceived the idea of the study. C.Y., C.C., J. Xia, X.J., J. Xu, X.Z. and S. Hou prepared the materials and performed electrochemical experiments. T.P.P, J.V. and O.B. conducted DFT and MD simulations. C.Y., A.F., J.A.D., M.T. and H.W. performed neutron scattering measurements. C.Y., A.K. and E.T. conducted activity coefficient measurements. C.Y., E.H., S. Hwang, D.S., Y.R. and X.-Q.Y. performed X-ray diffraction and scattering measurements. C.Y., C.C. and M.S.D. performed DSC measurements. C.Y. and W.S. performed XPS analysis. C.Y., O.B. and C.W. wrote the paper, and all authors contributed to editing the manuscript.

Competing interests

The authors declare no competing interests.

Additional information

Supplementary information The online version contains supplementary material available at https://doi.org/10.1038/s41893-022-01028-x.

Correspondence and requests for materials should be addressed to Oleg Borodin or Chunsheng Wang.

Peer review information *Nature Sustainability* thanks Andrzej Eilmes, Katja Kretschmer, Guanjie He and the other, anonymous, reviewer(s) for their contribution to the peer review of this work.